

# The molecular basis for SARS-CoV-2 recognized by dog ACE2

**Zengyuan Zhang**

Chinese Academy of Sciences

**Yanfang Zhang**

Chinese Academy of Sciences

**Kefang Liu**

Chinese Academy of Sciences

**Yan Li**

Chinese Academy of Sciences

**Qiong Lu**

National Institutes for Food and Drug Control (NIFDC),

**Qingling Wang**

Northwest University, Xi'an

**Yuqin Zhang**

Chinese Academy of Sciences

**Liang Wang**

Chinese Academy of Sciences

**Hanyi Liao**

Chinese Academy of Sciences

**Anqi Zheng**

Chinese Academy of Sciences

**Sufang Ma**

Chinese Academy of Sciences

**Zheng Fan**

Chinese Academy of Sciences

**Huifang Li**

The Northern Medical District of the PLA General Hospital

**Weijin Huang**

National Institutes for Food and Drug Control (NIFDC),

**Yuhai Bi**

Chinese Academy of Sciences

**Qihui Wang**

Chinese Academy of Sciences

**George F. Gao**

Chinese Academy of Sciences

**Haixia Xiao**

Chinese Academy of Sciences

**Jianxun Qi**

Chinese Academy of Sciences

**Yeping Sun** (✉ [sunyeping@im.ac.cn](mailto:sunyeping@im.ac.cn))

Institute of Microbiology, Chinese Academy of Sciences

---

## Article

**Keywords:** SARS-CoV-2, RBD/dACE2, crystal structure, binding interface mutations, affinity

**Posted Date:** March 2nd, 2021

**DOI:** <https://doi.org/10.21203/rs.3.rs-263301/v1>

**License:**   This work is licensed under a Creative Commons Attribution 4.0 International License.

[Read Full License](#)

---

**Version of Record:** A version of this preprint was published at Nature Communications on July 7th, 2021. See the published version at <https://doi.org/10.1038/s41467-021-24326-y>.

# Abstract

SARS-CoV-2 can infect many domestic animals, including dogs. Herein, we show that dog angiotensin converting enzyme 2 (dACE2) can bind to SARS-CoV-2 spike (S) protein receptor binding region (RBD), and that both pseudotyped and authentic SARS-CoV-2 can infect dACE2-expressing cells. We solved the crystal structure of RBD in complex with dACE2 and found that the total numbers of contact residues, contact atoms, hydrogen bonds and salt bridges at the binding interface in this complex are slightly fewer than those in the complex of the RBD and human ACE2 (hACE2). This result is consistent with the fact that the binding affinity of RBD to dACE2 is lower than that to hACE2. We further show that a few important mutations in the RBD binding interface play a pivotal role in the binding affinity of RBD to both dACE2 and hACE2, and need intense monitoring and controlling.

## Introduction

There is a continuously escalating threat from emerging and re-emerging viral diseases on human health<sup>1</sup>. The ongoing Coronavirus Disease 2019 (COVID-19) pandemic, caused by the SARS-CoV-2, again highlights the serious challenge faced by global public health. Up to January 27th, 2021, the number of confirmed COVID-19 cases have accumulated to more than 100 million, including over 2.1 million deaths<sup>2</sup>.

One possible origin of COVID-19 is the cross-species transmission of SARS-CoV-2 from animals to humans. SARS-CoV-2 shares a whole genome identity of 96% with a bat-derived CoV, BatCoV RaTG13, from *Rhinolophus affinis* in Yunnan Province, China<sup>3</sup>. In addition to BatCoV RaTG13, another SARS-CoV-2-like CoV, sharing 91.02% whole genome identity to SARS-CoV-2, was isolated from dead Malayan pangolins<sup>4</sup>. However, the S protein of neither BatCoV RaTG13 nor the pangolin SARS-CoV-2-like CoV harbors the functional polybasic (furin) cleavage site at the S1-S2 boundary found in the S protein of the SARS-CoV-2, which suggests that the virus may not directly jump from these two species to human. An observation of an intermediate or fully formed polybasic cleavage site in a SARS-CoV-2-like virus from animals would lend further support to identify the direct origin of the SARS-CoV-2<sup>5</sup>.

SARS-CoV-2 may have a wide range of animal hosts. Some domestic animals, including several pets that have close contacts with humans, are susceptible to the virus. For example, the virus was shown to replicate efficiently in ferrets and cats, but poorly in dogs<sup>6</sup>. A recent study gave evidence that angiotensin converting enzyme 2 (ACE2) from many animals, including *Primates* (monkey), *Lagomorpha* (rabbit), *Pholidota* (Malayan pangolin), *Perissodactyla* (horse), most *Carnivora* (cat, fox, dog, and raccoon dog) and most *Artiodactyla* (pig, wild Bactrian camel, bovine, goat and sheep) can bind to the SARS-CoV-2 S protein receptor binding domain (RBD), as their human counterpart, the human ACE2 (hACE2)<sup>7</sup>. hACE2 is the human receptor of SARS-CoV-2<sup>8,9,10</sup>, so SARS-CoV-2 may also exploit ACE2 from other animals as the receptor to infect these animals.

Dogs are one of the most popular domestic pets throughout the world and can have a close contact with humans. They could play a role in SARS-CoV-2 transmission if they can be infected. Indeed, dogs from households with confirmed human cases of COVID-19 in Hong Kong were confirmed to be infected with SARS-CoV-2, and genetic sequences of the viruses from the two dogs were identical to the virus detected in the respective human cases. The evidence suggests that these are instances of human-to-animal transmission of SARS-CoV-2 <sup>11</sup>. Recently, a large-scale of epidemiological survey that included 919 cats and dogs living in Italy showed that 3.3% of dogs and 5.8% of cats were SARS-CoV-2 neutralizing antibody positive, with dogs from COVID-19 positive households being significantly more likely to test positive than those from COVID-19 negative households <sup>12</sup>. These results further stress the potential risk of these pets in SARS-CoV-2 spreading.

To define the variance at SARS-COV-2 infection efficacies between dACE2- and hACE2-over expressed stable cells line, as well as to determine the interaction difference between RBD-dACE2 and RBD-hACE2 at atomic level, we tested the binding affinity of RBD and RBD mutants to dACE2 and to hACE2 by biochemical approach and further solved the crystal structures of RBD in complex with dACE2. Furthermore, we analyzed the residues of RBD, which involve in the interaction with either dACE2 or hACE2 in detail. With all these results and evidences, we demonstrate that a few important mutations in the RBD binding interface play a pivotal role in the binding affinity to dACE2 and hACE2.

## Results

### **Binding affinity of dACE2/hACE2 to RBD and infectivity of pseudotyped and authentic viruses**

SARS-CoV-2 S glycoprotein is a protein of 1273 residues. It harbors a furin cleavage site (Q677TNSPRRAR↓SV687) at the boundary between the S1/S2 subunits <sup>13</sup>. The S1 domain contains two subdomains, the N-terminal domain (NTD) and C-terminal domain (CTD). RBD is responsible for receptor recognition, which was mapped in previous structural studies <sup>9,10</sup>. dACE2 shares 83.88% primary sequence identity with hACE2. It is also composed of two subdomains, the subdomains I and II (Fig. 1A). Because of the high sequence consensus between hACE2 and dACE2, we speculated that dACE2 may also be able to bind to RBD. Therefore, we determined the binding affinities between RBD to hACE2 and to dACE2. The results show that the dissociation constant ( $K_D$ ) between RBD and hACE2 is 18.5 nM, while that between RBD and dACE2 is 123 nM, which confirms that dACE2 can indeed bind to RBD, but with a binding affinity 6.65 time lower than hACE2 (Fig. 1B and 1C).

To test the hypothesis that dACE2 is a receptor for SARS-CoV-2, we infected the BHK21 cells transfected dACE2 with a pseudovirus bearing SARS-CoV-2 S protein. Our results showed that the fluorescence signal represented as the relative luminescence units (RLU) in the S protein-expressing BHK21 cells has a dose-dependence relation with the virus dilutions. At the virus dilution of 60 and 180, the RLU values in the dACE2 expressing BHK21 cells are significantly higher than those in the BHK21 cells without expressing dACE2 ( $p < 0.0001$ , student's t-test), but at the virus dilutions lower than 180, no statistic difference between the BHK21 cells expressing dACE2 and without expressing dACE2 is observed (Fig. 1D). In

contrast, the SARS-CoV-2 S protein-bearing pseudovirus infection leads to significantly higher RLU values in the hACE2-expressing BHK21 than in those without expressing hACE2 (Fig. 1E). These results suggest that the pseudovirus bearing the SARS-CoV-2 S protein can infect the dACE2 expressing cells, but with a less efficiency than infect the hACE2 expressing cells. They are consistent to our SPR results showing that the affinity of SARS-CoV-2 S protein to dACE2 is lower than to hACE2 (Fig. 1B and 1C).

When infected with the authentic SARS-CoV-2, the number of copies of the SARS-CoV-2 ORF1ab significantly increase in the HeLa cells expressing either dACE2 or hACE2 at 48 and 72 h after infection, compared with those not expressing these two molecules (Fig. 1F). These results confirm that dACE2 is indeed a cellular receptor that supports SARS-CoV-2 infecting host cells, just as its human ortholog, the hACE2.

### **The Overall Structure Of DACE2 In Complex With RBD**

In order to elaborate the structural basis for dACE2 binding to RBD, we determined the crystal structure for the RBD/dACE2 complex (Fig. S1A). The RBD/dACE2 complex was prepared with size exclusion chromatography and the structure was solved to 3.0 Å resolution (Table S1), with one RBD binding to a single dACE2 molecule in the asymmetric unit. For dACE2, clear electron densities could be traced for 596 residues from S19 to Y706 and L721 to G725 as well as glycans N-linked to residue N342, while the electron densities for R707 to S720 is invisible. The structure for RBD in the complex includes residues T333 to P526, all of which have clear density. The overall structure of RBD/dACE2 is very similar to previously reported RBD/hACE2 (PDB ID: 6LZG) with a RMSD of 0.654 (Fig. S1B).

The RBD in the RBD/dACE2 complex structure protein shows the same fold with that in the SARS-CoV-2-RBD/hACE2 complex previous reported. It is divided into two subdomains: the  $\beta$ -sheet-dominated conserved core domain, which is stabilized by a disulfide bond between  $\beta$ c2 and  $\beta$ c4, and the loop-dominated external domain, which contains two small  $\beta$ -sheets. The dACE2 also share similar architecture with hACE2 in the RBD/hACE2 complex: it is divided into subdomain I, which interact with RBD and subdomain II, the catalyzing subdomain (Fig S1C and S1D).

### **The interaction interface between dACE2 and RBD and comparison with the RBD/hACE2 complex**

We analyzed the atomic contacts between dACE2 and RBD in the crystal structure of dACE2/RBD with a cutoff distance of 4 Å. In the complex, 18 dACE2 residues (Q19, L23, T26, F27, E29, K30, Y33, E36, E37, Y40, Q41, T81, Y82, E325, N329, K352, D354 and R356) form atomic contacts with 18 RBD residues (R403, K417, G446, Y449, Y453, L455, F456, A475, F486, N487, Y489, G496, Q498, T500, N501, G502, Y505 and Q506) (Fig. 2A). The total number of atomic contacts between dACE2 and RBD is 127 (Table S2 and S3). Among these contacts, 118 are Van der Waals (vdw) interactions, and 14 are hydrogen bonds (H-bonds) or salt bridges (Table S2 and S3). The contact interface in RBD has a saddle shape with two protrusive side parts and a recessed center part, and can be divided into two contact regions (CRs), CR1 (R403, G446, Y449, Q498, T500, N501, G502 and Q506) and CR2 (K417, Y453, L455, F456, F486, N487 and Y489) (Fig. 2C-2D). CR1 is mainly composed of polar residues. In this region, K403 forms a hydrogen bond with dACE2 residue Y33; Q498 forms hydrogen bonds with dACE2 residues E37, Q41 and K352; and

G502 forms hydrogen bonds with K352 (Fig. 2C). Other polar atomic contacts between CR1 and dACE2 include G446 interacting with Q41, Y449 with E37 and Q41, G502 with G353, and Q506 with E325.

Different from the CR1, the CR2 is mainly composed of hydrophobic and aromatic residues. In CR2, residue K471 forms a salt bridge with dACE2 E29; N487 forms a hydrogen bond with Y82 (Fig. 2C). Other atomic contacts between CR2 and dACE2 involves CR2 Y453 interacting with dACE2 H34, N487 with L23, L455 with E29 and H33, F456 with T26 and E29, F486 with T81 and T82, and Y489 with T26 F27, K30 and Y82 (Fig. 2C). Generally, the RBD CR1 and CR2 interact with two overlapping contact regions in dACE2, CR1' and CR2', respectively (Fig. 2A and 2C).

In comparison, in the crystal structure of RBD/hACE2 complex, 20 residues in hACE2 (S19, Q24, T27, F28, D30, K31, H34, E35, E37, D38, Y41, Q42, Q45, M82, Y83, N330, K353, G354, D355, R357) form atomic contacts with 19 RBD residues (K417, G446, Y449, Y453, L455, F456, A475, G476, F486, N487, Y489, F490, Q493, G496, Q498, T500, N501, G502, Y505). To be noticed, the residue T20 in hACE2 is missing in dACE2, so the residue number of dACE2 is one less than hACE2 after position 20 (Fig. S2). The total number of atomic contacts between RBD and hACE2 is 145, among which 16 are hydrogen bonds or salt bridges (Table S2 and S3). Compared with the RBD in the RBD/dACE2 structure, the CR1 (G446, Y449, G496, Q498, T500, N501 and G502) of the RBD in the RBD/hACE2 structure does not include R403 and Q506, but includes G496 which the former does not include; and the CR2 (K417, Y453, L455, F456, A475, F486, N487, Y489, F490, and Q493) includes F490, A475 and Q493 which the CR2 in the RBD/dACE2 structure does not include. In the RBD/hACE2 structure, the RBD CR1 residue Y449 forms a H-bond with hACE2 residues D38 and Q42; G496 forms a H-bond with K353; Q498 forms a H-bond with Q42, N501 forms a H-bond with Y41, and G502 forms a H-bond with K352. Besides, CR1 T500 forms strong vdw contacts with Y41, N330, D355, R357. In CR2 of this structure, K417 also forms a salt bridge with hACE2 D30; A475 forms a H-bond with S19; N487 forms a H-bond with Q24 and Y83. Other atomic contacts between CR2 and hACE2 include CR2 Y453 and L455 interacting with hACE2 H34, F456 with T27, D30, K31; F486 with M82 and Y83; F490 with K31; and Q493 with H34 and E35. The contact residues in hACE2 can also be grouped into two contact regions, CR1' and CR2', which are not overlapping (Fig. 2B and 2D).

We further analyzed the difference in the interface residue contacts at specific positions of dACE2 and hACE2 (Fig. 3). It revealed that dACE2 S19 only makes a vdw contact with SARS-CoV-2 RBD, while hACE2 S19 not only makes vdw contacts with A475 and G476, but also forms a hydrogen bond with A475 (Fig. 3A). Moreover, dACE2 L23 makes 3 vdw contacts with A475 and N487, but the corresponding hACE2 Q24 forms a hydrogen bond with N487 and 7 vdw contacts with A475 and N487 (Fig. 3B). dACE2 E29 forms a hydrogen bond and a salt bridge with K417, and the corresponding hACE2 D30 forms a hydrogen bond and two salt bridges with K417 (Fig. 3C). Additionally, dACE2 Y33 interacts with R403, Y453 and L455, while hACE2, whereas the corresponding hACE2 H34 interact with Y453, L455 and Q493 (Fig. 3D). Furthermore, dACE2 E34 does not contact with any SARS-CoV-2 RBD residue, whereas the corresponding hACE2 E35 contacts with Q493 (Fig. 3E). What is more, dACE2 E325 interacts with N501 and Q506, whereas the corresponding hACE2 G326 does not contact with any SARS-CoV-2 RBD residue (Fig. 3F).

In summary, slightly fewer residues are involved in forming the interaction interface in the SARS-CoV-2 RBD/dACE2 complex (18 SARS-CoV-2 RBD residues and 18 dACE2 residues) than those in the SARS-CoV-2 RBD/hACE2 complex (19 SARS-CoV-2 RBD residues and 20 dACE2 residues, and the total number of atom contacts, hydrogen bonds and salt bridges in the SARS-CoV-2 RBD/dACE2 (127, 13, 1, respectively) are also less than those in the SARS-CoV-2 RBD/hACE2 complex (145, 15, 2, respectively).

### **Effect of RBD interface residue mutations on its binding affinity to dACE2 or hACE2**

As mentioned above, at the RBD/dACE2 and RBD/hACE2 interfaces, there is a conserved salt bridge, which is formed by RBD K417 and hACE D30 or dACE E29. Salt bridges are among the strongest non-covalent bonds in protein interface interactions. To address the role of these salt bridges on the affinity of the binding partners, we introduced K417V or K417N mutations which are found in some SARS-CoV-2 isolates (Fig. S3A) to RBD and examined the binding affinity of these mutants to hACE2 and dACE2 by Surface plasmon resonance (SPR). The results showed that the  $K_D$  of RBD with K417V and K417N mutations to dACE2 are 400 nM and 507 nM, respectively (Fig. 4A and 4B). Compared to the  $K_D$  of the wide type (wt) RBD to dACE2 (123 nM, Fig. 1C), these values are 3.25 and 4.12 times higher, respectively, suggesting that the salt bridge disruption significantly reduces the affinity of RBD to dACE2. Similarly, the  $K_D$  of RBD with K417V and K417N to hACE2 are 53.4 nM and 49.7 nM (Fig. 4E and 4F), which near 3 times decrease compared to the binding affinity the wt RBD to hACE2 (Fig. 1B). These results confirm that the disruption of the conserved salt bridge indeed reduces the affinity of RBD to both dACE2 and hACE2.

To be noticed, the  $K_D$  value of RBD N501Y mutant, which is also detected in SARS-CoV-2 stains (Fig. S3B), binding to dACE2 and hACE2 are 37.1 and 0.881 nM (Fig. 4C and 4G), which are 3.32 and 21.00 times less than those of wt RBD to dACE2 and hACE2, respectively. Therefore, N501Y mutation enhances the affinity of RBD to both dACE2 and hACE2, among which, the augment is specifically significant for hACE2.

To confirm the effect of RBD mutations on the binding capacity to native formatted ACE2, we measured the binding of RBD mutants to ACE2s expressed on 293T cell surface by flow cytometer (Fig. 4D, 4H and S4). The results show that the percentage of the RBD K417N mutant-binding dACE2-positive HEK293T cells was significantly lower than that of wt RBD binding dACE2-positive cells. Whereas, the percentage of the RBD N501Y mutant binding dACE2-positive HEK293T cells was significantly higher than that of wt RBD binding dACE2-positive cells. Similarly, among hACE2-positive HEK293T cells, the percentage of both the RBD K417N and K417V mutant-binding cells were significantly lower than that of the wt RBD-binding cells, while the RBD N501Y mutant-binding cells was significantly higher than that of the wt RBD-binding cells. These results again confirmed the importance of RBD interface residues at positions 417 and 501 for determination of the binding affinity to both dACE2 and hACE2 receptors.

## **Discussion**

The findings that SARS-CoV-2 can infect domestic animals have raised a concern that these animals could be a neglected transmission route of this virus <sup>14</sup>. Previous evidence has shown that dog can be naturally infected with SARS-CoV-2 <sup>11,15</sup>, and dACE2 can bind to RBD <sup>4</sup>. In the present study, we solved the crystal structure of the RBD/dACE2 complex, and revealed the molecular basis for SARS-CoV-2 recognizing its receptor in dogs. We found that the overall structures of RBD/dACE2 are very similar to the RBD/hACE2 complex. However, the interaction interface of these two complexes are slightly different. The numbers of contact atoms, residues, hydrogen bonds in the RBD/dACE2 interface, are slightly less than those in the RBD/hACE2, which explains the 6.65 times lower affinity of dACE2 to RBD as compared with hACE2 (Fig. 1B).

We further showed that the naturally occurring interface residue mutations, including K417V, K417N, and N501Y, can significantly modified the affinity of dACE2/hACE2 to RBD. Among them, K417V and K417N, which destroy the sole salt bridge in the interface, reduce the affinity, while N501Y increases the affinity. These results confirm the importance of these interface contact residues, and they also validate the interface residue contact information generated from our crystal structures. Notably, the N501Y mutation not only renders SARS-CoV-2 infectivity to mouse, which is not susceptible to wt SARS-CoV-2 <sup>16</sup>, but also significantly increases the RBD affinity to dACE2 and hACE2 (Fig. 4). These factors mean that N501Y mutation could become a strategy applied by the virus to adapt various animal species and acquire a wider host range. Actually, N501Y mutation has been detected in SARS-CoV-2 isolated from humans, and the number of virus isolates bearing this mutation keep increasing. Up to Feb. 1st 2021, there have been 37367 N501Y mutation containing strains reported around the world <sup>17</sup>. Hence, this mutation should be closely monitored in naturally circulated strains of SARS-CoV-2.

Apart from the three mutations which we investigated, some other SARS-CoV-2 RBD interface residue mutations that modify the affinity of RBD to hACE2 have recently been reported. Some of them increase the affinity to the hACE2 receptor, such as V367F, W436R, N354D/D364Y <sup>18</sup>. In addition to N501Y, the naturally occurring N501F and N501T also increase the affinity of RBD to hACE2. There is no evidence that shows that they have been selected in current SARS-CoV-2 pandemic isolates <sup>19</sup>. However, these studies suggest that N501 may be a mutation 'hotspot' for the virus to acquire adaptability to the host. These RBD interface residue mutations highlight the necessity to closely monitor virus evolution and to take consideration during vaccine development.

SARS-CoV-2 can spread from human to animals, including cats and dogs <sup>20</sup> and spreads among cats <sup>21</sup>. Furthermore, this virus can transmit from human to mink and transmit back to human <sup>22</sup>. Up to now, no evidence has shown that the virus has gained the ability to transmit from cats or dogs to humans. However, our results here show that N501Y mutation can remarkably increase the affinity of RBD to dACE2, and quite possibly in turn increases the transmissibility of the virus. Therefore, monitoring binding affinity of animal ACE2 to RBD can provide precaution for occurrence of any new transmission chain and opportunities to nip it in the bud.

# Materials And Methods

## Protein expression and purification

The codon-optimized sequences for ectodomains of dACE2 (S19-T739) was cloned into pET21a vector and overexpressed as inclusion bodies in the BL21 (DE3) strain of *Escherichia coli*. Renaturation and purification of dACE2 was done as previous reported<sup>4, 23, 24</sup>. Briefly, the dACE2 inclusion bodies solved in 6 M urea were dropwise injected and diluted of in the L-arginine refolding buffer. After 24 h, the renatured proteins were purified by a Superdex™ 200 Increase 10/300 GL column (GE Healthcare)<sup>25, 26</sup>. Refolded dACE2 was used for RBD/dACE2 crystallization and SPR assay.

Moreover, codon-optimized sequences dACE2 (S19- T739) was fused with mouse Fc and cloned into pCAGGS vector. To purify hACE2-mFc, pCAGGS-hACE2-mFc was transfected into HEK 293F cells. After 5 days' expression, the protein was purified by HiTrap Protein A FF (GE Healthcare) affinity chromatography column and further purified by Superdex™ 200 Increase 10/300 GL column (GE Healthcare). hACE2-mFc was used for SPR.

SARS-CoV-2 RBD was expressed as previous reported<sup>4, 10, 27</sup>. The gene cloned into the Bac-to-Bac baculovirus expression vector was recombined with the baculovirus. The recombinant baculovirus was then purified and used to infect Hi5 cells. The supernatant collected from the cell culture was filtered through a 0.22 µm filter membrane and the protein with a His tag was purified with a His-Trap HP column (GE Healthcare). Then, the protein was further purified by a Superdex™ 200 Increase 10/300 GL column (GE Healthcare).

## SPR Analysis

SPR measurements were performed using BIAcore 8000 system (GE Healthcare) with CM5 chips as previous reported (GE Healthcare)<sup>28</sup>. The buffer for all the proteins in the SPR analysis was HBST (20 mM 4-(2-Hydroxyethyl) piperazine-1-ethanesulfonic acid (HEPES), 150 mM NaCl, pH 7.4). HBST was also used as the running buffer.

2799 units hACE2 and 6566 units dACE2 were immobilized on the CM 5 chip, respectively. RBD was serially diluted (6.25 to 100 nM or 25 to 400 nM, for hACE2 and dACE2, respectively) and flowed over these two channels. After each cycle, the sensor surface was regenerated with HBST buffer. The RBD K417N and K417V mutants of serial concentrations from 125 nM to 2000 nM and were flowed over the channel immobilized with 6400 units dACE2. The RBD K417N and K417V mutants of serially concentrations from 25 nM to 400 nM and from 31.25 nM to 500 nM, respectively, were flowed over the channel immobilized with 7500 units hACE2. RBD N501Y was serially diluted to concentrations of 3.125 nM to 50 nM or 25 nM to 400 nM, and was then flowed over the channels immobilized with 6688 units hACE2 or 5881 units dACE2, respectively. The data were analyzed by the Biacore™ Insight evaluation software (GE healthcare) using a 1:1 Langmuir binding model.

## Pseudovirus Infection Assay

Pseudotyped SARS-CoV-2 particles prepared with the VSV pseudotyped virus packaging system were provided by Weijin Huang from the National Institute for Food and Drug Control. The virus titer was  $10^{5.8}$  TCID<sub>50</sub>/mL as previously reported<sup>29</sup>. The plasmids of full length hACE2 and dACE2 tagged with eGFP at C terminal were transfected into BHK21 cells, respectively. After 24 h, the eGFP-positive cells were sorted by flow cytometry, seeded in 96-well plates ( $1 \times 10^4$  cells per well) and then cultured at 5% CO<sub>2</sub>, 37 °C for 24 h. Three-fold serial dilutions of the pseudovirus were added to the GFP positive cells. After 24 h, cells were washed with PBS for twice and lysed with the Luciferase Assay System reagent (Promega). The luciferase activity was measured using a GloMax 96 Microplate luminometer (Promega), and the data were analyzed using GraphPad Prism 6.0 software.

### **Live Virus Infection Assay**

HeLa cells overexpressed with hACE2 and dACE2 on cell membrane were inoculated with SARS-CoV-2 (hCoV-19/China/CAS-B001/2020, GISAID databases EPI\_ISL\_514256-7) at a multiplicity of infection (MOI) of 0.005, and incubated for 1 h at 37 °C. The virus inoculum was then washed twice and replaced with fresh medium DMEM. Culture supernatants were harvested at 2, 24, 48, and 72 h and then used to extract viral RNA. The viral ORF1ab copies were tested by quantitative RT-PCR (forward primer: CCCTGTGGGTTTTACTTAA, reverse primer: ACGATTGTGCATCAGCTGA, fluorescent probe [P]: 5'- the FAM-CCGTCTGCGGTATGTGGAAAGGTTATGG-BHQ1-3') according to the manual of One Step PrimeScript™ RT-PCR kit.

### **Flow Cytometry Analysis**

For flow cytometry analysis, HEK293T cells were transfected with the full length dACE2 and hACE2 fused with eGFP and incubated in 5% CO<sub>2</sub> at 37°C for 48 h. Then,  $2 \times 10^5$  cells were resuspended, collected and incubated with RBD or MERS-CoV RBD proteins of a concentration of 5 µg/mL at 37°C for 30 min. After that, the cells were washed three times with PBS and stained by anti-His/APC antibody (1:500, Miltenyi Biotec) at 37°C. After 30 min incubation, the cells were washed three times with PBS, and analyzed using BD FACSCanto. The assays were independently performed three times.

### **Statistics Analysis**

The virus infection and flow cytometry data were analyzed by one-way analysis of variance (ANOVA), while the differences between two groups were analyzed using Student's t test. A probability value of  $p < 0.05$  was considered statistically significant.

### **Crystallization, Data Collection, And Structure Determination**

The sitting-drop method was used to obtain high-resolution crystals<sup>30, 31, 32</sup>. In detail, the RBD/dACE2 complex protein was concentrated to 7.5 mg/mL, and 0.8 µL protein was mixed with 0.8 µL reservoir solution. The resulting solution was sealed and equilibrated against 100 µL of reservoir solution at 18°C.

The high-resolution crystals were grown in 2% 1,4-dioxane, 0.1 M tris pH 8.0, 15% polyethylene glycol 3,350.

Diffraction data were collected at the Shanghai Synchrotron Radiation Facility (SSRF) BL19U. The dataset was processed using HKL2000 software<sup>33</sup>. The structure of RBD/dACE2 complex was determined by the molecular replacement method using Phaser<sup>34</sup>, with previously reported complex structure RBD complex with hACE2 (PDB: 6LZG). The atomic models were completed with Coot<sup>35</sup> and refined with phenix.refine in Phenix<sup>34</sup>, and the stereochemical qualities of the final models were assessed with MolProbity<sup>36</sup>.

## Declarations

### ACKNOWLEDGEMENTS

This work was supported by the National Key Research and Development Program of China (2018YFC1200603, 2016YFD0500305, 2020YFC0845900), the Strategic Priority Research Program of CAS (XDB37030204), and the National Natural Science Foundation of China (31800775).

We thank Dr. Tong Zhao from the center of public technology service in Institute of Microbiology, Chinese Academy of Sciences for assistance in flow cytometry assay.

### AUTHOR CONTRIBUTIONS

Y.S., J.Q., H.X. and G.F.G conceived and supervised the study. Z.Z., Y.Z., H.L., H.L. and A.Z. prepared protein samples, carried out SPR and cytometry assay. Z.Z., Y.Z., K.L. S.M. and Q.W. performed the crystal structure studies. Z. F. L.W. and Q.W. did the SPR assay. Y.L., Y.B., Q. L., W.H. and Z.Z. carried out virus assay.

### DECLARATION OF INTERESTS

The Authors declare no competing interests.

## References

1. Gao GF. From "A" IV to "Z"IKV: attacks from emerging and re-emerging pathogens. *Cell* **172**, 1157–1159. (2018).
2. The Johns Hopkins Coronavirus Resource Center COVID-19 Dashboard by the Center for Systems Science and Engineering (CSSE) at Johns Hopkins. <https://coronavirus.jhu.edu/map.html>. Accessed on January 27th, 2021.
3. Zhou P, *et al.* A pneumonia outbreak associated with a new coronavirus of probable bat origin. *Nature* **579**, 270–273. (2020).

4. Zhang T, Wu Q, Zhang Z. Probable pangolin origin of SARS-CoV-2 associated with the COVID-19 outbreak. *Curr Biol* **30**, 1346–1351 e1342. (2020).
5. Andersen KG, Rambaut A, Lipkin WI, Holmes EC, Garry RF. The proximal origin of SARS-CoV-2. *Nat Med* **26**, 450–452. (2020).
6. Shi J, *et al.* Susceptibility of ferrets, cats, dogs, and other domesticated animals to SARS-coronavirus 2. *Science* **368**, 1016–1020. (2020).
7. Wu L, *et al.* Broad host range of SARS-CoV-2 and the molecular basis for SARS-CoV-2 binding to cat ACE2. *Cell discovery* **6**, 68. (2020).
8. Shang J, *et al.* Structural basis of receptor recognition by SARS-CoV-2. *Nature* **581**, 221–224. (2020).
9. Lan J, *et al.* Structure of the SARS-CoV-2 spike receptor-binding domain bound to the ACE2 receptor. *Nature* **581**, 215–220. (2020).
10. Wang Q, *et al.* Structural and functional basis of SARS-CoV-2 entry by using human ACE2. *Cell* **181**, 894–904 e899. (2020).
11. Sit THC, *et al.* Infection of dogs with SARS-CoV-2. *Nature* **586**, 776–778. (2020).
12. Patterson EI, *et al.* Evidence of exposure to SARS-CoV-2 in cats and dogs from households in Italy. *Nat Commun* **11**, 6231. (2020).
13. Walls AC, Park YJ, Tortorici MA, Wall A, McGuire AT, Veesler D. Structure, Function, and Antigenicity of the SARS-CoV-2 Spike Glycoprotein. *Cell* **181**, 281–292 e286. (2020).
14. Hernandez M, Abad D, Eiros JM, Rodriguez-Lazaro D. Are animals a neglected transmission route of SARS-CoV-2? *Pathogens* **9**, 480. (2020).
15. Abdel-Moneim AS, Abdelwhab EM. Evidence for SARS-CoV-2 infection of animal hosts. *Pathogens* **9**, 529. (2020).
16. Gu H, *et al.* Adaptation of SARS-CoV-2 in BALB/c mice for testing vaccine efficacy. *Science* **369**, 1603–1607. (2020).
17. China National Center for Bioinformation 2019 Novel Coronavirus Resource (2019nCoV-VR). <https://bigd.big.ac.cn/ncov/variation/annotation/variant/23063?lang=en>. Accessed on February 7th, 2020.
18. Ou J, *et al.* Emergence of SARS-CoV-2 spike RBD mutants that enhance viral infectivity through increased human ACE2 receptor binding affinity. *bioRxiv*, DOI: <https://doi.org/10.1101/2020.03.15.991844>. (2020).
19. Starr TN, *et al.* Deep Mutational Scanning of SARS-CoV-2 Receptor Binding Domain Reveals Constraints on Folding and ACE2 Binding. *Cell* **182**, 1295–1310 e1220. (2020).
20. Bosco-Lauth AM, *et al.* Experimental infection of domestic dogs and cats with SARS-CoV-2: Pathogenesis, transmission, and response to reexposure in cats. *Proc Natl Acad Sci U S A* **117**, 26382–26388. (2020).
21. Halfmann PJ, *et al.* Transmission of SARS-CoV-2 in Domestic Cats. *N Engl J Med* **383**, 592–594. (2020).

22. Oude Munnink BB, *et al.* Transmission of SARS-CoV-2 on mink farms between humans and mink and back to humans. *Science* **371**, 172–177. (2020).
23. Liu K, *et al.* Structural basis of anti-PD-L1 monoclonal antibody avelumab for tumor therapy. *Cell Research* **27**, 151–153. (2017).
24. Tan S, *et al.* Crystal clear: visualizing the intervention mechanism of the PD-1/PD-L1 interaction by two cancer therapeutic monoclonal antibodies. *Protein & Cell* **7**, 866–877. (2016).
25. Lu D, *et al.* Peptide presentation by bat MHC class I provides new insight into the antiviral immunity of bats. *PLoS Biology* **17**, e3000436. (2019).
26. Zhang Q, *et al.* Strict Assembly Restriction of Peptides from Rabbit Hemorrhagic Disease Virus Presented by Rabbit Major Histocompatibility Complex Class I Molecule RLA-A1. *Journal of Virology* **94**, e00396-00320. (2020).
27. Liu K, *et al.* Cross-species recognition of SARS-CoV-2 to bat ACE2. *Proc Natl Acad Sci U S A* **118**, e2020216118. (2021).
28. Liu K, *et al.* N-glycosylation of PD-1 promotes binding of camrelizumab. *EMBO Reports*, e51444. (2020).
29. Nie J, *et al.* Quantification of SARS-CoV-2 neutralizing antibody by a pseudotyped virus-based assay. *Nat Protoc* **15**, 3699–3715. (2020).
30. Zhao M, Zhang H, Liu K, Gao GF, Liu WJ. Human T-cell immunity against the emerging and re-emerging viruses. *Science China Life sciences* **60**, 1307–1316. (2017).
31. Zhang Y, *et al.* Evaluation of Zika Virus-specific T-cell Responses in Immunoprivileged Organs of Infected *Ifnar1*<sup>-/-</sup> Mice. *Journal of visualized experiments: JoVE*, 58110. (2018).
32. Liu K, Meng, Y., Chai, Y., Li, L., Sun, H., Gao, G.F., Tan, S., Qi, J. Crystal structure of the African swine fever virus core shell protein p15. *Biosafety and Health*, DOI: <http://dx.doi.org/10.1016/j.bsheal.2020.09.002>. (2020).
33. Otwinowski Z, Minor W. [20] Processing of X-ray diffraction data collected in oscillation mode. *Methods in Enzymology* **276**, 307–326. (1997).
34. Adams PD, *et al.* PHENIX: a comprehensive Python-based system for macromolecular structure solution. *Acta crystallographica Section D, Biological crystallography* **66**, 213–221. (2010).
35. Emsley P, Cowtan K. Coot: model-building tools for molecular graphics. *Acta crystallographica Section D, Biological crystallography* **60**, 2126–2132. (2004).
36. Williams CJ, *et al.* MolProbity: More and better reference data for improved all-atom structure validation. *Protein science: a publication of the Protein Society* **27**, 293–315. (2018).
37. Kumar S, Stecher G, Li M, Knyaz C, Tamura K. MEGA X: molecular evolutionary genetics analysis across computing platforms. *Mol Biol Evol* **35**, 1547–1549. (2018).
38. Robert X, Gouet P. Deciphering key features in protein structures with the new ENDscript server. *Nucleic Acids Res* **42**, W320-324. (2014).

# Figures

## Figure 1

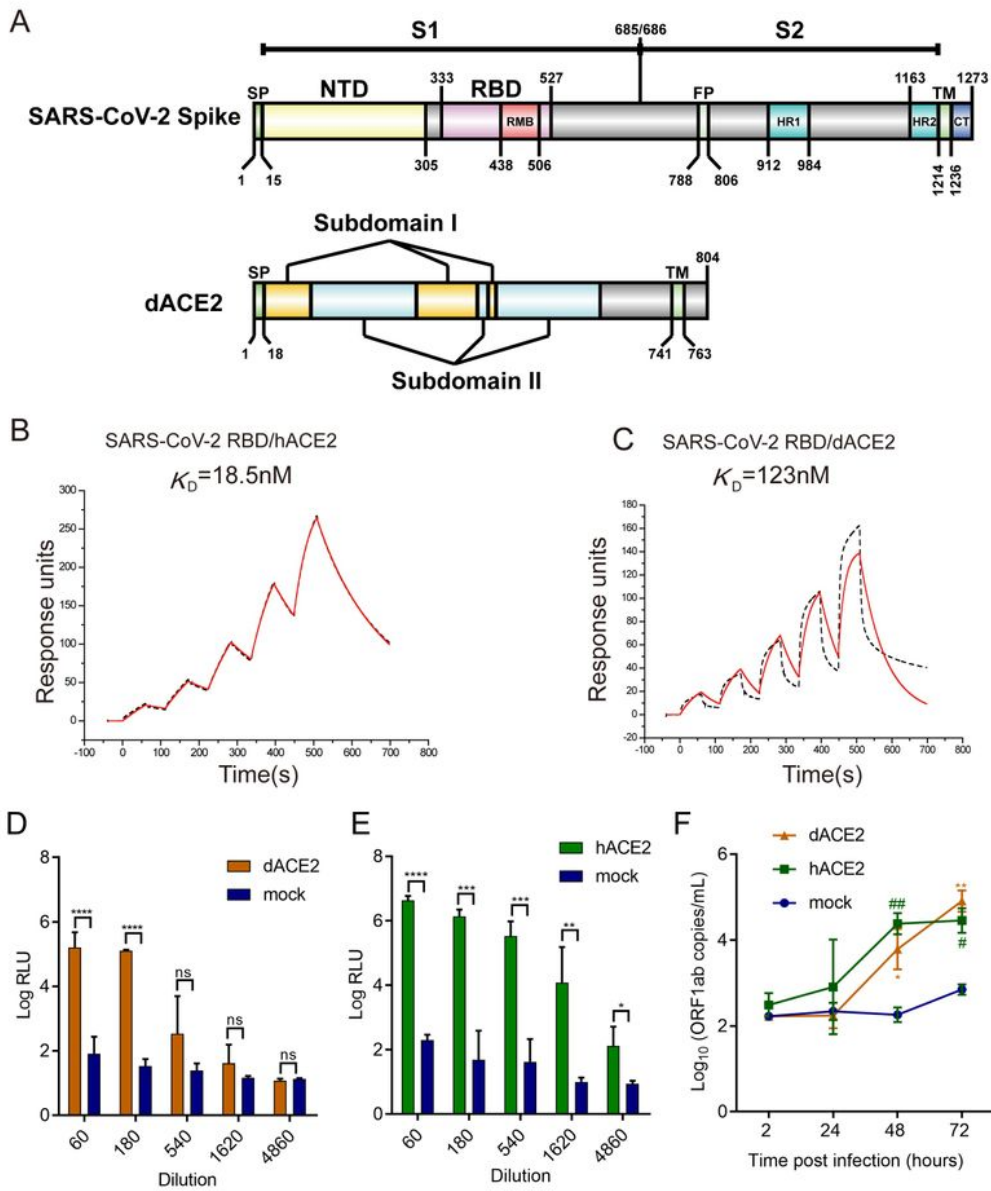


## Figure 1

The binding affinity of RBD to both dACE2 and dACE2, and the infection efficacies of pseudovirus in dACE2- and dACE2-expressing BHK21 stable cells. . (A) Schematic of SARS-CoV-2 S (first panel) and dACE2 (second panel) linear compositions colored by domain. (B) SPR binding curves for immobilized

hACE2 with the soluble RBD. (C) SPR binding curves for immobilized dACE2 with the RBD. The black dash lines represent the actual data, while the red solid lines represent the fitted results (B and C). (D) Infection of dACE2-expressing BHK21 cells with SARS-CoV-2 S protein-bearing pseudovirus. (E) Infection of hACE2-expressing BHK21 cells with SARS-CoV-2 S protein-bearing pseudovirus. P values were calculated with t-test, \*\*\*\* p < 0.0001, \*\*\* p < 0.001, \*\* p < 0.01, \* p < 0.05, ns means no significant differences. (F) Infection of dACE2/hACE2-expressing HeLa cells with SARS-CoV-2 authentic virus. \*\* p < 0.01, \* p < 0.05 vs mock; ## p < 0.01, # p < 0.05 vs mock; Student's t-tests.

**Figure 2**

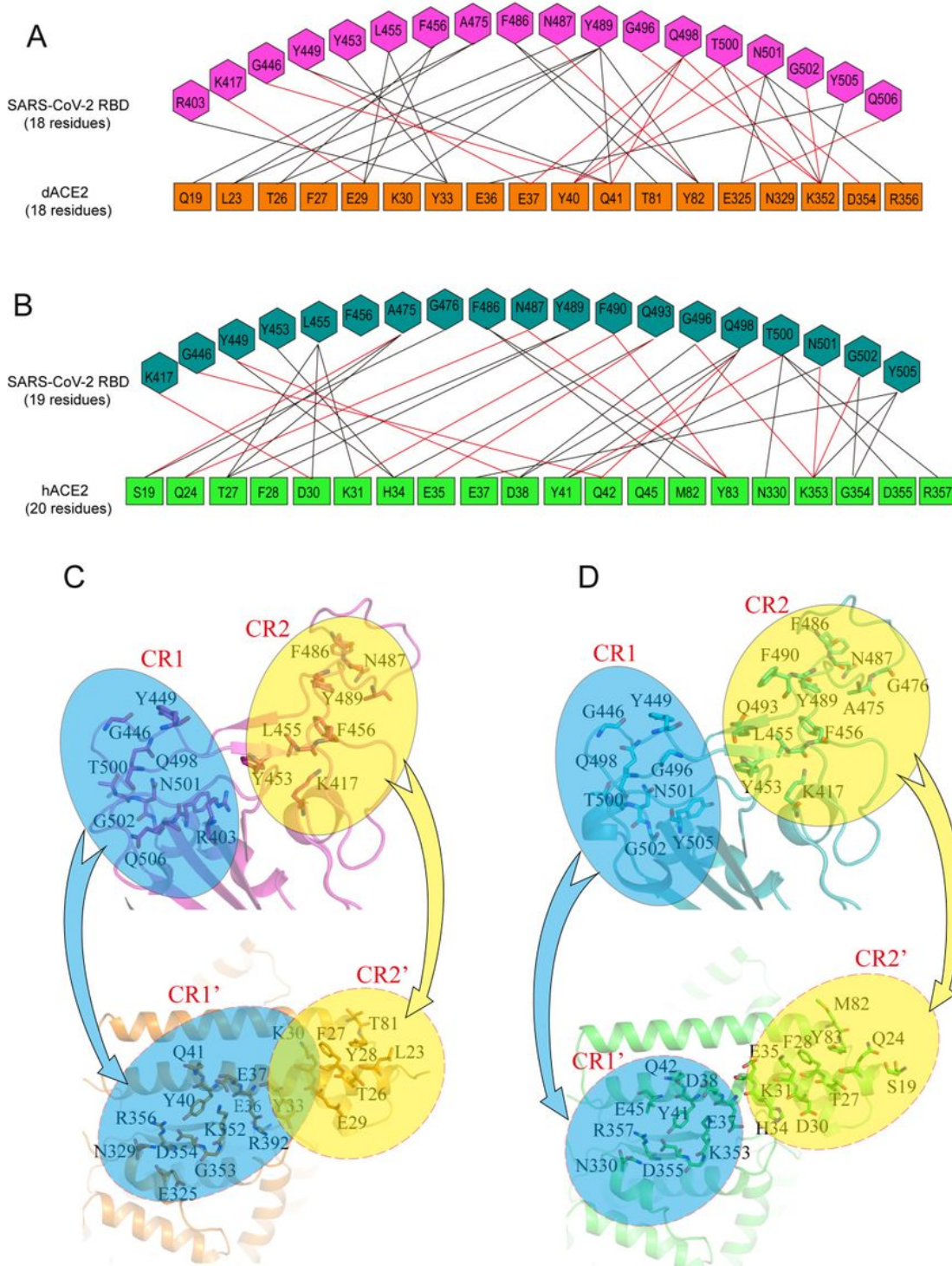


## Figure 2

Interaction interface in the RBD/dACE2 complex and the RBD/hACE2 complex (PDBID: 6LZG). (A) Residue interactions in the RBD/dACE2 interface. (B) Residue interactions in the RBD/hACE2 interface. The black lines represent vdw interactions, and the red lines represent hydrogen bonds or salt bridges (A and B). (C) The residues involved in interface interactions in the RBD/dACE2 complex. (D) The residues involved in interface interactions in the RBD/hACE2 complex. The interaction interface in RBD is divided into two contact regions (CR1 and CR2), and their corresponding contact regions in residues in dACE2 (C) or hACE2 (D) are named CR1' and CR2', respectively. The residues involved in interface contacts are shown as the stick representation (C and D).

Figure 3

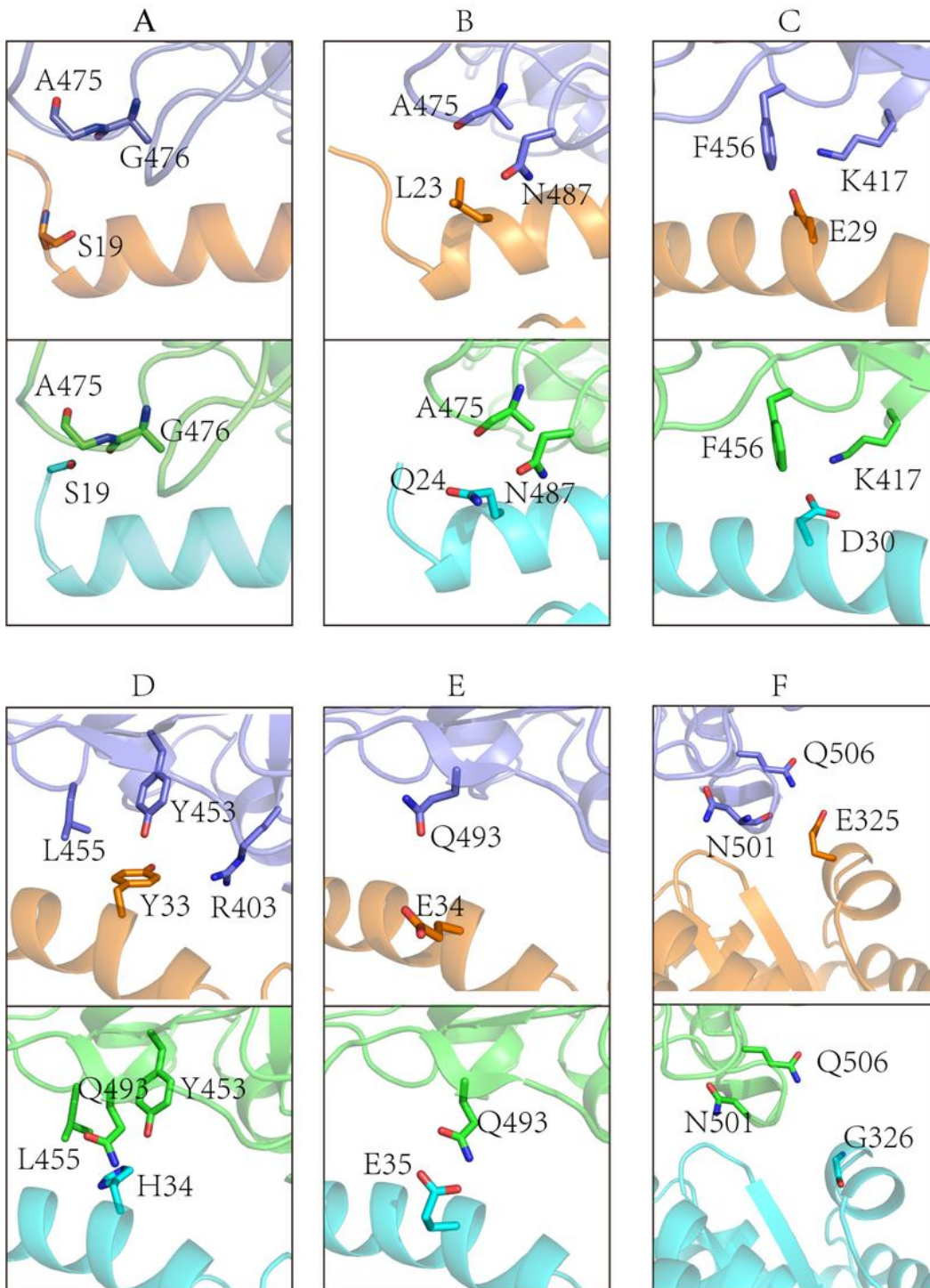
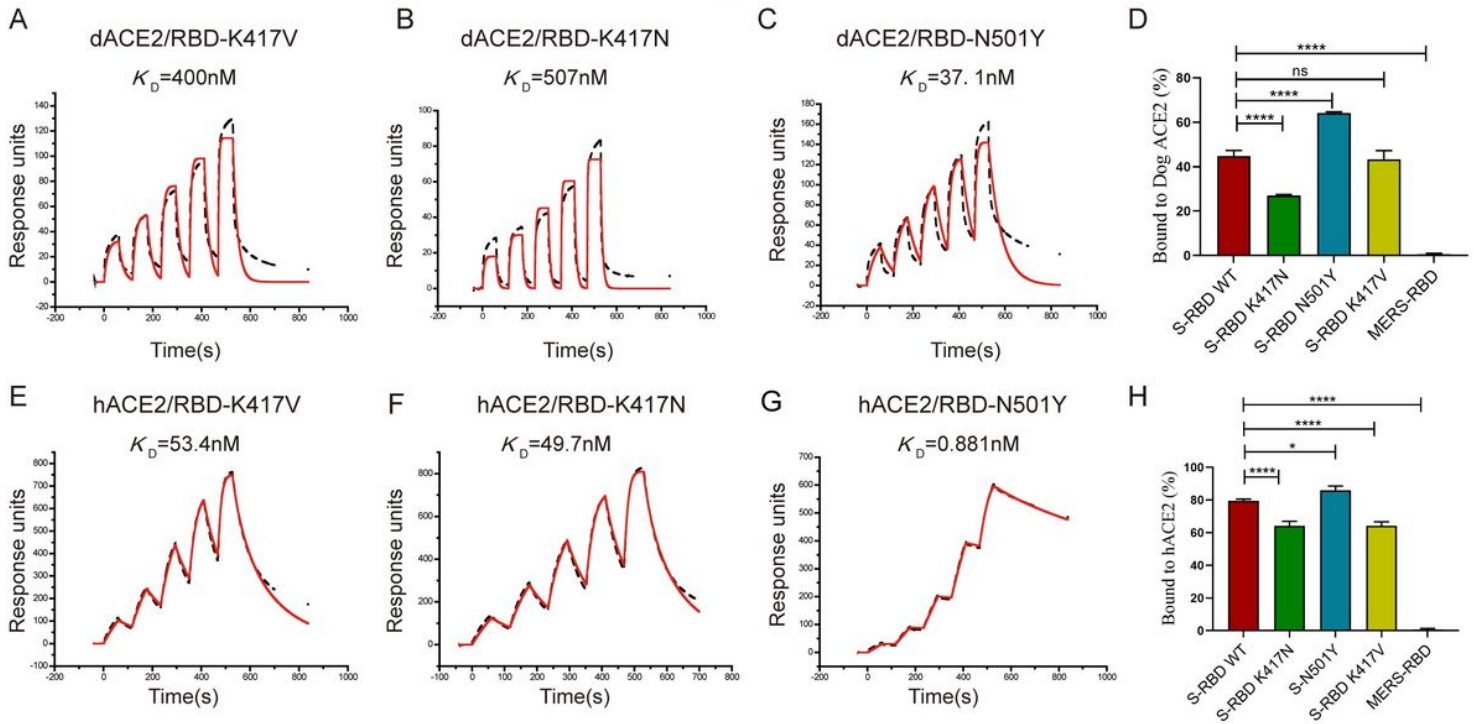


Figure 3

Comparison of interface residue contacts at specific positions of dACE2 and hACE2. In the RBD/dACE2 complex (A-F upper panels), RBD residues are colored in light blue, and dACE residues are colored with orange. In the RBD/hACE2 complex (A-F lower panels), RBD residues are colored with green, and dACE residues are colored in cyan.

# Figure 4



**Figure 4**

Binding ability of RBD mutants to both soluble and transmembrane dACE2 and hACE2. (A-C) SPR sensorgram for RBD interface residue mutants binding to hACE2. (E-G) RBD interface residue mutants binding to dACE2. The black dash lines represent the actual data, while the red solid lines represent the fitted results. The  $K_D$  value for each mutant is indicated. (D) and (H) Flow cytometry assay for RBD interface residue mutants binding to dACE2 (D) and hACE2 (H). The percentage of Y-axis represent the percentage of the APC+EGFP+ cells in the EGFP+ cells. The results shown here represent Mean $\pm$ SD for 3 independent experiments. \*,  $p<0.05$  vs WT; \*\*\*\*,  $p<0.001$  vs WT; student's t-tests.

## Supplementary Files

This is a list of supplementary files associated with this preprint. Click to download.

- [tableS1.docx](#)
- [tableS2.docx](#)
- [tableS3.docx](#)
- [FigS1.tif](#)
- [FigS2.tif](#)
- [FigS3.tif](#)
- [FigS4.tif](#)